Supplement of Atmos. Chem. Phys., 25, 15715–15740, 2025 https://doi.org/10.5194/acp-25-15715-2025-supplement © Author(s) 2025. CC BY 4.0 License.





Supplement of

Formation of highly oxygenated organic molecules from α -pinene photooxidation: evidence for the importance of highly oxygenated alkoxy radicals

Sungah Kang et al.

Correspondence to: Sören R. Zorn (s.zorn@fz-juelich.de)

The copyright of individual parts of the supplement might differ from the article licence.

S1. Experimental details

5

10

Experiments without CO and NO addition were performed as reference case. In these experiments $J(O^1D)$ was altered by the gap of the UVC lamp, thus the OH· source strength. The steady state concentrations of α -pinene, O_3 , and OH· radicals served as a test for the model calculations. The temperature varied between 290 K and 291 K and relative humidity (RH) varied between 62.6% and 61.8%.

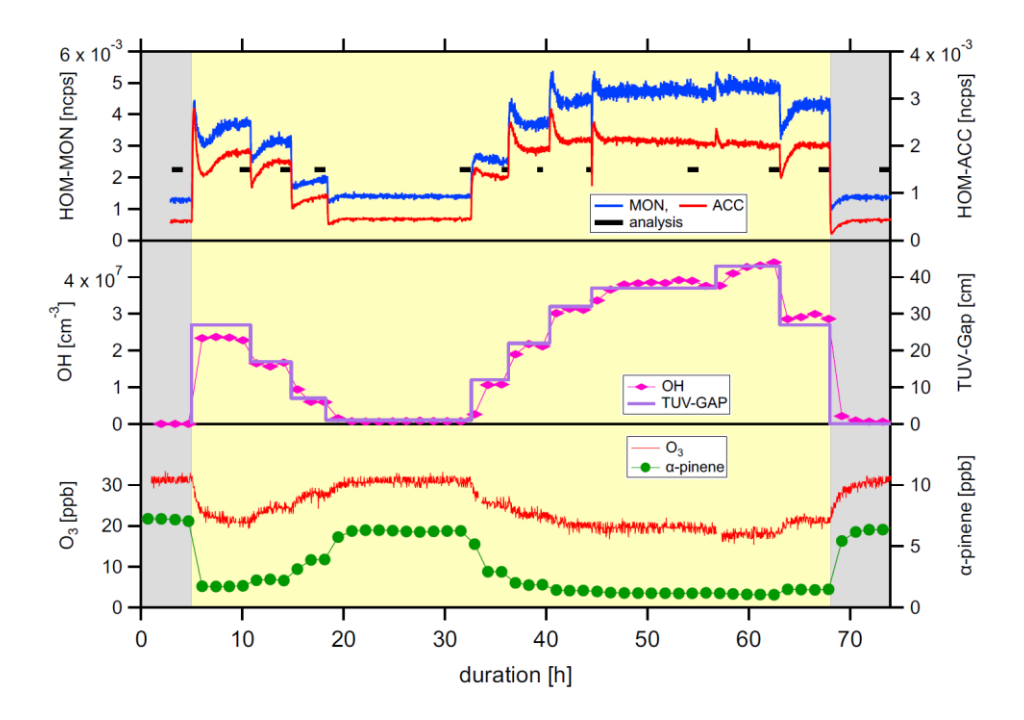


Figure S1: Overview over the reference experiment. Steady state periods which were chosen for analysis are indicated by the black bars in the upper panel. $[OH\cdot]_{ss}$ follows the TUV-gap in the mid panel very well, i.e. the width of the opening through which UVC-light enters the chamber.

The NO_X experiments were conducted over a period of 31 days. An overview for a single NO_X experiment is shown in Fig. S2. NO was added with UVC-light switched off (grey background), while UVA-light was always on. The photochemistry was started by switching on the UVC light, as indicated by the yellow background. In the NO_X experiments α -pinene, O_3 , NO, NO_2 and OH_{\cdot} , concentrations at steady state were compared to the model calculations. The average temperature for 13 of the 14 days when experiments were performed was 288.4 ± 0.1 K with RH= $70\pm0.7\%$. At the very first experiment day the temperature was only 287 K and the RH 77.5%. Within the 14 experiments we repeated two experiments, and one other pair resulted in very similar NO concentrations, despite different initial conditions in NO_X and O_3 . These data were pairwise averaged, such that we end up with 11 data points with CIMS and NO_X measurements. The reproducibility was $\pm8-14\%$, essentially owed to imperfections in exactly reproducing the experimental boundary conditions.

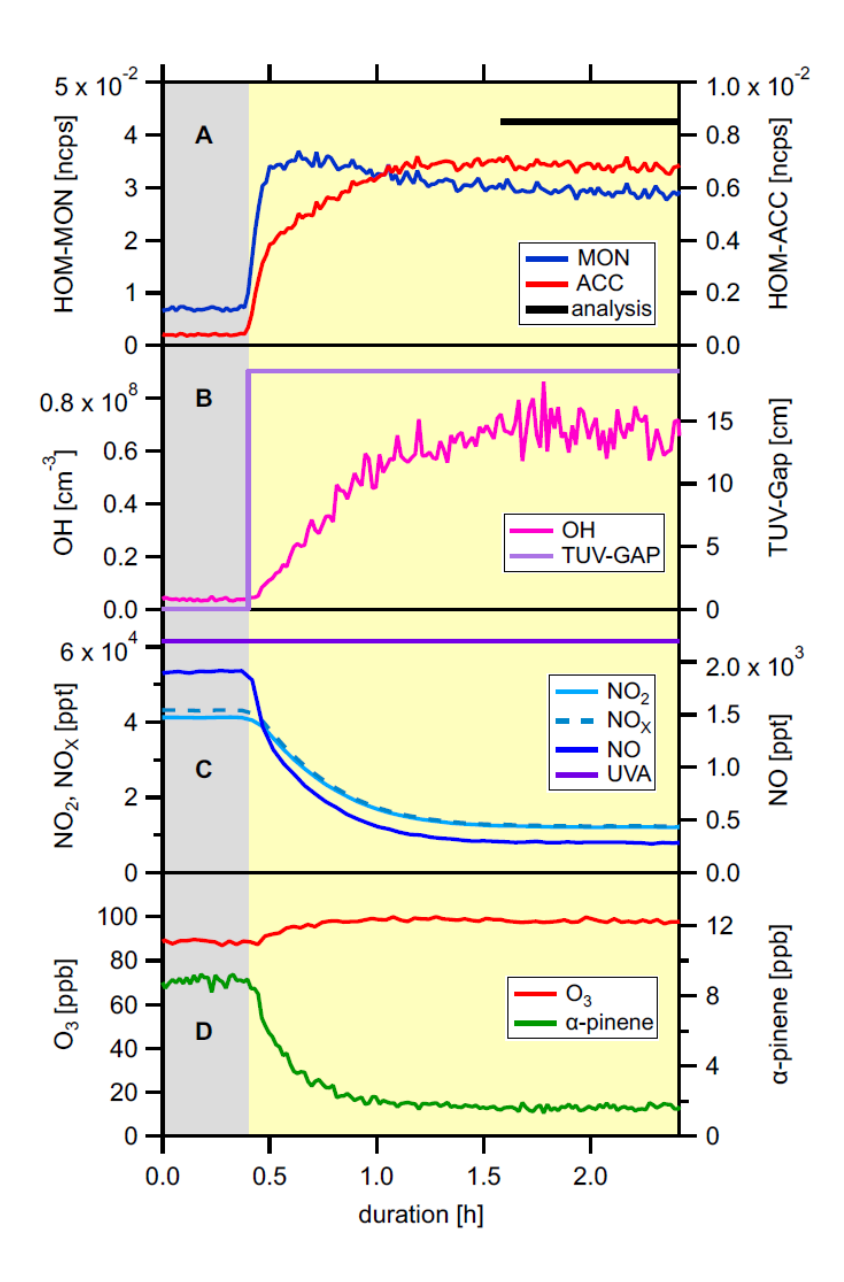


Figure S2: Overview over a single NO_X experiment. The steady state period that was chosen for analysis is indicated by the black bar in the upper panel. The photochemistry indicated by the increase of the OH-radical concentration started when the UVC-light was switched on. TUV-gap was held at 19 cm throughout all NO_X experiments.

Table S1 shows an overview of the parameters of all experiments.

Table S1:	Experimental	Parameters

Nr.	Input	[α-pinene] _{ss} [ppb]	[O ₃] _{ss} [ppb]	[OH·] _{ss} [cm ⁻³]	[NO] _{ss} [ppt]	[NO ₂] _{ss} [ppb]	Turnover ^a [cm ³ s ⁻¹]
J1	UVC off	7.1	30.7	$8.1 \cdot 10^{05}$	<1	< 0.3	$7.88 \cdot 10^{06}$
J2	UVC off	6.3	30.5	$9.4 \cdot 10^{05}$	<1	< 0.3	$8.20 \cdot 10^{06}$
Ј3	Gap = 1 cm	6.2	30.2	$1.7 \cdot 10^{06}$	<1	< 0.3	$1.45 \cdot 10^{07}$
J4	Gap = 6 cm	3.9	27.2	$7.8 \cdot 10^{06}$	<1	< 0.3	$4.19 \cdot 10^{07}$
J5	Gap = 11 cm	2.16	24.5	$2.0 \cdot 10^{07}$	<1	< 0.3	$5.77 \cdot 10^{07}$
J6	Gap = 15 cm	2.21	24.1	$2.0 \cdot 10^{07}$	<1	< 0.3	$6.09 \cdot 10^{07}$
J7	Gap = 20 cm	1.8	22.2	$2.4 \cdot 10^{07}$	<1	< 0.3	$6.14 \cdot 10^{07}$
J8	Gap = 24 cm	1.7	20.8	$3.1 \cdot 10^{07}$	<1	< 0.3	$6.21 \cdot 10^{07}$
J9	Gap = 24 cm	1.5	21.1	$2.8 \cdot 10^{07}$	<1	< 0.3	$6.62 \cdot 10^{07}$
J10	Gap = 29 cm	1.3	20.1	$3.7 \cdot 10^{07}$	<1	< 0.3	$6.65 \cdot 10^{07}$
J11	Gap = 33 cm	1.1	19.4	$4.3 \cdot 10^{07}$	<1	< 0.3	$6.71 \cdot 10^{07}$
J12	Gap = 39 cm	1	18.3	$4.8 \cdot 10^{07}$	<1	< 0.3	$6.74 \cdot 10^{07}$
C1	CO ≈ 5 ppm	5.5	36	1.10^{07}	<1	< 0.2	$7 \cdot 10^{07}$

Nr.	Input	[α-pinene] _{ss} [ppb]	[O ₃] _{ss} [ppb]	[OH·]ss [cm ⁻³]	[NO]ss [ppt]	$\begin{array}{c} [NO_2]_{ss} \\ [ppb] \end{array}$	[NO _X] _{ss} [ppb]
N1 ^b	NO = 0.0 ppb	2.8	59.5	$3.8 \cdot 10^{07}$	2	0.3	0.3
N2	NO = 7.0 ppb	2.4	65.1	$4.7 \cdot 10^{07}$	38	1.7	1.8
$N3^{b}$	NO = 15.2 ppb	2.3	70.1	$4.9 \cdot 10^{07}$	131	3.7	3.8
N4 ^b	NO = 24.8 ppb	1.8	81.0	$6.1 \cdot 10^{07}$	144	5.2	5.4
N5	NO = 39.2 ppb	1.8	82.4	$6.1 \cdot 10^{07}$	277	8.4	8.7
N6	NO = 45.2 ppb	1.7	92.1	$6.7 \cdot 10^{07}$	276	10.1	10.4
N7	NO = 51.8 ppb	1.7	97.9	$6.9 \cdot 10^{07}$	343	12.2	12.5
N8	NO = 60.7 ppb	2.1	91.8	$5.0 \cdot 10^{07}$	586	15.3	15.9
N9	NO = 82.8 ppb	2.3	95.7	$4.6 \cdot 10^{07}$	1010	25.0	26.0
N10	NO = 97.1 ppb	2.5	98.7	$4.3 \cdot 10^{07}$	1344	33.6	35.0
N11	NO = 138 ppb	4.1	83.8	$2.1 \cdot 10^{07}$	3967	70.5	74.5

 $^{^{}a}\ k_{OH}\cdot [OH]\cdot \left[\alpha\text{-pinene}\right]$ $^{b}\ average\ of\ 2\ experiments$

S2. Corrections of the HOM signal for loss on particles and varying turnover by OH-

35

40

45

60

Sarrafzadeh et al. (2016) show that in experiments with varying $[NO_X]$ new particle formation and changes of OH, respectively VOC turnover by OH, can mask the effect of NO_X itself. The experiments presented here were conducted in a way that new particle formation was suppressed as much as possible, however at the highest OH concentrations in the reference experiments and at low NO_X in the NO_X experiments some particles were still being formed. In the NO_X experiments we tried to keep the variation of the α -pinene turnover small by choosing suitable combinations of NO- and O_3 -input.

Following Pullinen et al. (2020) we referenced the observed HOMs to a particle free chamber by considering the extra loss to the particle surface in addition to the wall loss, with the loss coefficients L_P and L_W , respectively. The corresponding correction factor P_{corr} is given by

$$P_{corr} = \frac{L_W + L_P}{L_W} \tag{S1}$$

 L_W was determined from the lifetime = 120 s of HOM $C_{10}H_{16}O_7$ with the molecular mass of 248 Da. L_P was approximated for the molecular properties of $C_{10}H_{16}O_7$, observed mode diameter and total surface S_{tot} of the particle surface distribution, and the temperature in the chamber.

$$L_p = F_{corr} \cdot \frac{\bar{c}}{4} \cdot S_{tot} \qquad (S2)$$

In (S2) F_{corr} is the Fuchs-Sutugin correction factor (Fuchs ans Sutugin, 1971), and \bar{c} is the mean molecular velocity of $C_{10}H_{16}O_7$ at the chamber temperature. P_{corr} can be applied to all HOM because the square root of the molecular mass that enters \bar{c} and the diffusion coefficient cancels out.

The observed HOM can be referenced to a reference turnover by considering the power law dependence of the total HOM signal on the α-pinene turnover (Pullinen et al., 2020). Here we define as total HOM signal the sum of all signals attributed to the formula compounds in the peak list. Figure S3 shows the total HOM signal (particle corrected applying (S1)) of the experiments J1-J12 and N1-N11 as a function of the turnover. A power law fitted to data from J4-J11, where the fraction of turnover with OH· was larger than 90%, results in a slope of 2.0. The data N1-N11 are located almost perfectly on the extrapolated power law fit. The finding suggests that the HOM concentration increases quadratically with the turnover. As the reference turnover we chose 6.7·10⁷ cm⁻³ s⁻¹, the largest turnover in the exp. J1 - J12. The OH· correction factor for an experiment with a certain turnover is then given by equation (S3):

$$OH_{corr} = \left(\frac{6.7 \cdot 10^7}{turnover}\right)^2 \tag{S3}$$

We assume that the corrections can be applied independently, and that the signals referenced to a particle free chamber and a turnover of $6.7 \cdot 10^7$ cm⁻³ s⁻¹ are given by (S4):

$$signal_{corr} = P_{corr} \cdot OH_{corr} \cdot signal_{meas}$$
 (S4)

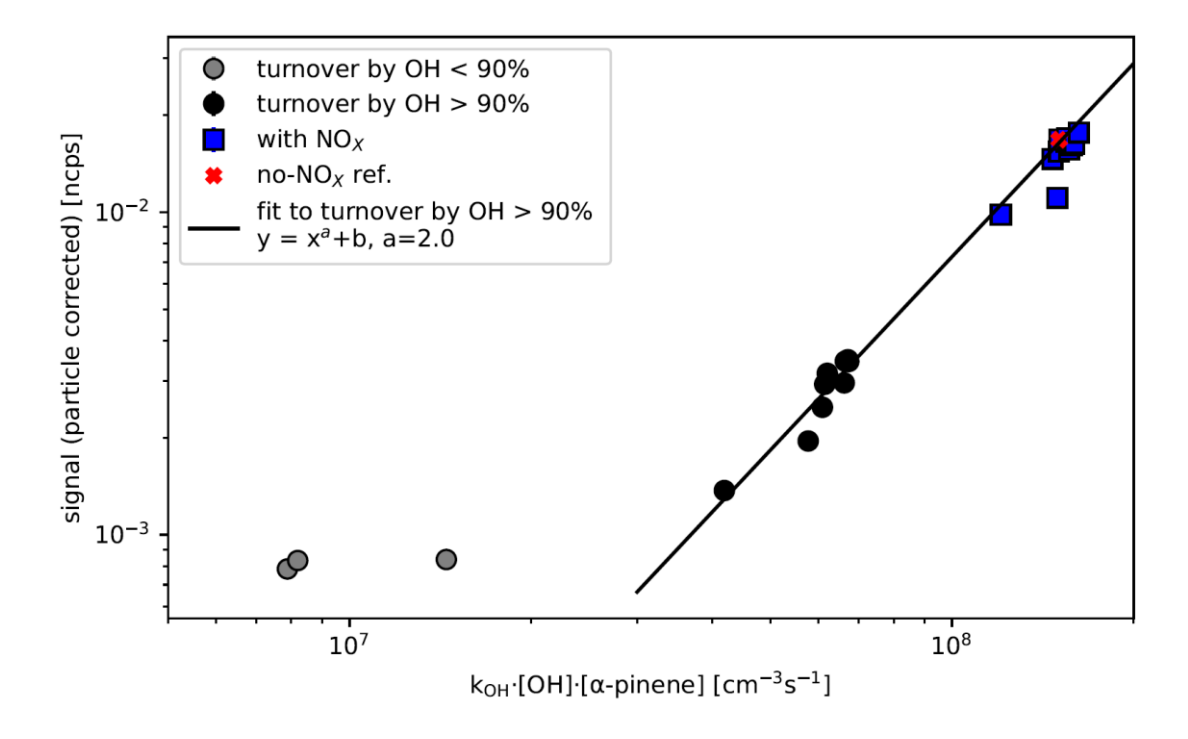


Figure S3: Determination of the OH· correction factor. Total HOM signal is plotted as a function of the apinene turnover with OH·. Experiments J1-J12 are given as filled circles, wherein black circles indicate primary turnover with OH· > 90%. The black line is a power law fit to the exp. J4-J12 which resulted in a quadratic dependence of the HOM signal on the turnover. The blue squares represent the NO_X exp. N2-N11, the $no-NO_X$ reference experiment N1 is indicated by the red cross. Standard deviations of the signal averaged over the steady state periods are smaller than the symbol size.

S3. Estimation of the RO₂· and HO₂· concentrations by model calculations

The concentrations of RO_2 · and HO_2 · in our experiments were estimated by box model calculations. For that we performed box model calculations adapting the gas-phase mechanism for α -pinene from MCMv3.3.1 to the boundary and initial conditions of JPAC (Table S2). The model calculations were performed by applying the institute package EASY, which is based on FACSIMILE (v. 3.05, 1993, AEA Technology plc) and IDL (v. 8.5.1, Exelis Visual Information Solutions, Inc.). In order to check the model performance, we compared the model output to measured $[\alpha$ -pinene]_{ss}, $[O_3]_{ss}$, and $[OH\cdot]_{ss}$, and as well to $[NO]_{ss}$ and $[NO_2]_{ss}$ where it applied (Figure S4).

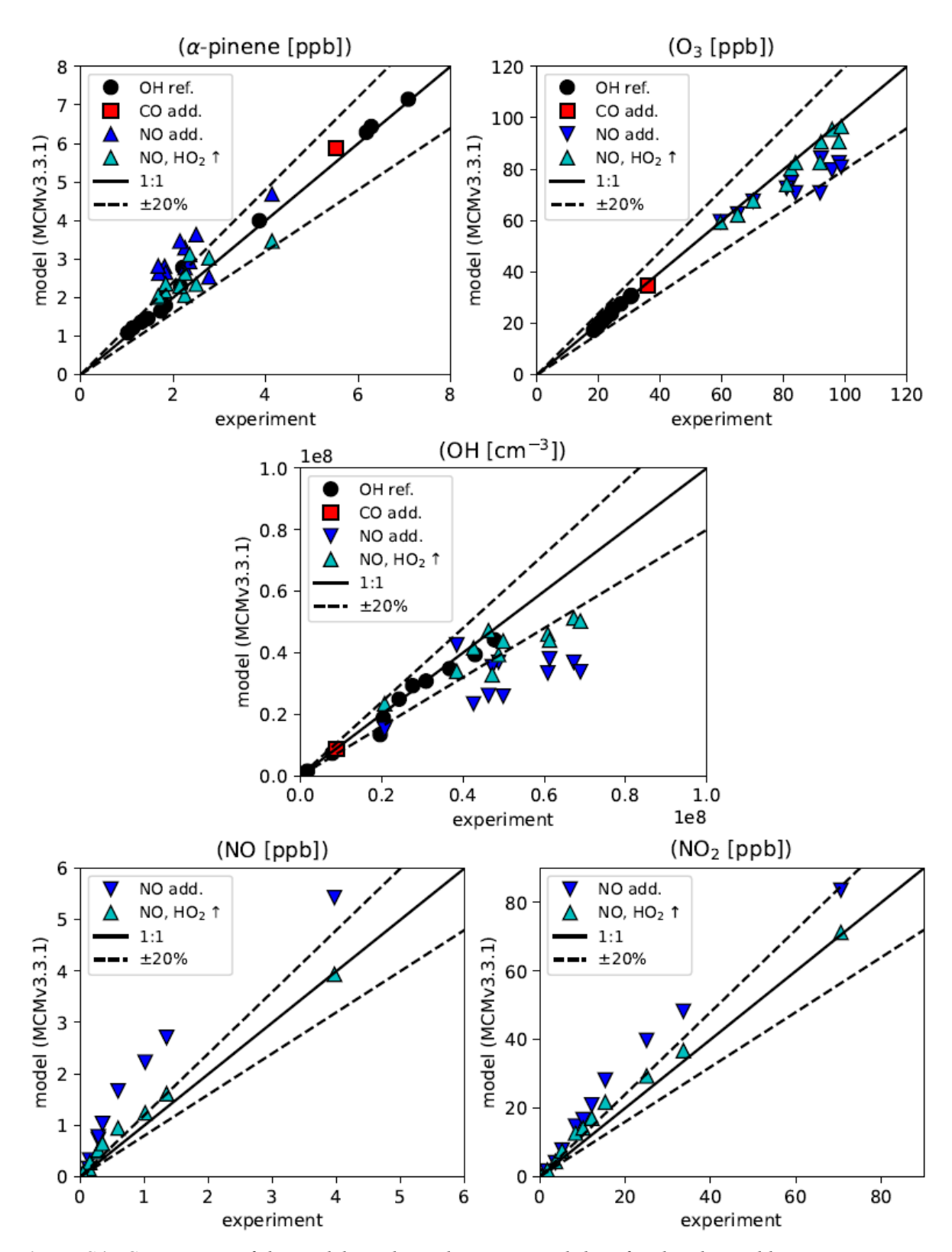


Figure S4: Comparison of the model results and experimental data for the observables α -pinene, ozone, $OH \cdot NO$ and NO_2 . In the case of the NO experiments in a second model run an $HO_2 \cdot$ source was mimicked by converting every $OH \cdot$ radical that is lost due to background reactivity (6 s⁻¹) to one gas-phase $HO_2 \cdot$ radical.

Table S2: Model Input Parameters

Nr	Flow [l·min ⁻¹]	T [K]	RH [%]	[α-pinene] [ppb]	[O ₃] [ppb]	[NO _X] [ppb]	$\begin{matrix} J_{O1D} \\ [s^{\text{-}1}] \end{matrix}$	$\begin{matrix} J_{NO2} \\ [s^{-1}] \end{matrix}$
J1	31.52	290.2	60.5	9.3	63.1	0.3	UVC off	0
J2	31.52	290.2	60.5	8.3	63.1	0.3	UVC off	0
Ј3	31.52	290.2	60.5	8.9	63.1	0.3	$1.00 \cdot 10^{04}$	0
J4	31.52	290.2	60.5	9.1	63.1	0.3	$7.10 \cdot 10^{04}$	0
J5	31.52	290.2	60.5	8.8	63.1	0.3	$1.22 \cdot 10^{03}$	0
J6	31.52	290.2	60.5	9.1	63.1	0.3	$1.73 \cdot 10^{03}$	0
J7	31.52	290.2	60.5	8.8	63.1	0.3	$2.25 \cdot 10^{03}$	0
Ј8	31.52	290.2	60.5	9.2	63.1	0.3	$2.76 \cdot 10^{03}$	0
Ј9	31.52	290.2	60.5	8.4	63.1	0.3	$2.76 \cdot 10^{03}$	0
J10	31.52	290.2	60.5	8.7	63.1	0.3	$3.27 \cdot 10^{03}$	0
J11	31.52	290.2	60.5	8.6	63.1	0.3	$3.78 \cdot 10^{03}$	0
J12	31.52	290.2	60.5	8.5	63.1	0.3	$4.39 \cdot 10^{03}$	0
C1ª	39.3	289.0	66.0	12.5	51	0.3	$2.67 \cdot 10^{03}$	0
Nr	Flow [l·min ⁻¹]	T [K]	RH [%]	[α-pinene] [ppb]	[O ₃] [ppb]	[NO _X] [ppb]	J _{O1D} [s ⁻¹]	J _{NO2} [s ⁻¹]
N1	35.45	287.6	74.2	18	83.3	0.0	2.15·10 ⁻⁰³	1.3·10 ⁻⁰³
N2	35.43	288.2	70.8	18.2	85.3	7.0	$2.15 \cdot 10^{-03}$	1.3·10 ⁻⁰³
N3	35.25	288.3	70.6	18.1	93.3	15.2	$2.27 \cdot 10^{-03}$	$1.3 \cdot 10^{-03}$
N4	35	288.3	70.3	18.2	100.1	24.8	$2.15 \cdot 10^{-03}$	$1.3 \cdot 10^{-03}$
N5	34.6	288.5	69.4	17.9	109.8	39.2	$2.15 \cdot 10^{-03}$	$1.3 \cdot 10^{-03}$
N6	35.1	288.5	69.6	18.1	128.1	45.2	$2.15 \cdot 10^{-03}$	$1.3 \cdot 10^{-03}$
N7	35.4	288.5	69.6	18	129.1	51.8	$2.15 \cdot 10^{-03}$	$1.3 \cdot 10^{-03}$
N8	35.2	288.2	70.3	18	121.9	60.7	$2.15 \cdot 10^{-03}$	$1.3 \cdot 10^{-03}$
N9	34.6	288.5	71	17.9	156.8	82.8	$2.15 \cdot 10^{-03}$	$1.3 \cdot 10^{-03}$
N10	35.5	288.4	69.9	18.1	168.1	94.1	$2.15 \cdot 10^{-03}$	$1.3 \cdot 10^{-03}$
N11	34.5	288.2	70.9	17.9	200.9	137.6	2.15·10 ⁻⁰³	1.3·10 ⁻⁰³

^a CO input 5 ppm

Since we are using outside air treated by catalytic oxidation and adsorption drying there remained some impurities in the experiment air. We observed a background of 300 ppt NO_X and 15 ppb CO in the inlet air. This was considered in all model calculations, as well as a background OH· reactivity of 4 s⁻¹ in the experiments J1-J12, C1 and of 6 s⁻¹ in the NO_X experiments N1-N11.

The model calculations for the no-NO_X cases, i.e. the variation of J(O¹D) and the CO addition produced very good results, whereas in case of high NO_X the gross trends were acceptable but neither NO, OH·, nor O₃ could be well reproduced at high NO_X additions. (Fig. S4). Problems in modelling photochemistry in simultaneous presence of high NO_X and of high VOC are well known, e.g. from field observations in China (Fuchs et al., 2017; Slater et al., 2020; Tan et al., 2017; Tan et al., 2018). It is related to not-understood radical sources and possibly incompleteness of the MCMv3.3.1 in these cases (Whalley et al., 2021). We tested constant simple sources for RO₂· and HO₂· in the model assuming that the background reactivity for OH· results either in RO₂ radicals with similar reactivity as propylperoxy, or in HO₂· radicals. The RO₂· source degraded the agreement and was not further pursued, while the HO₂· source led to improvement as shown in Figure S4.

Unfortunately, the observables in the no-NO_X experiments were not very sensitive to the extra HO₂· source, only at the highest OH· concentrations the agreement between modelled and observed [O₃]_{ss}, [OH·]_{ss}, and [α -pinene]_{ss} degraded significantly (not shown). The degradation could be mainly attributed to the reaction OH· + HO₂· which is a sink for OH·. In presence of the extra HO₂· source in the model this reaction seems to become too fast at the highest OH· concentrations and overcomes the OH· source by O₃ + HO₂·. This finding suggests that the HO₂· missing in the model in the NO_X/VOC experiments does not arise from a general chamber source but is related to the NO_X containing chemical system. Since the reason for the missing HO₂· is not quite clear we will adhere to the direct MCMv3.1.1 results (blue down pointing triangles in Figure S4). In view of these limitations, we used the modelled [RO₂·]_{ss}, [HO₂·]_{ss} (Table S3) and measured [NO]_{ss} together with the measured [HOM-RO₂·]_{ss} only for some simple relative kinetic estimations under steady state conditions. Since the RO₂· + NO reaction dominates at higher [NO_X]_{ss}, the tenor of argumentation in Section 3.4 of the main article is not affected by this choice, as only the relative importance of the minor HOM-RO₂· + RO₂· and HOM-RO₂· + HO₂· reactions would be modified at low NO.

Table S3: Model derived concentration of peroxy and hydroperoxy radicals								
Nr	RO ₂ · [cm ⁻³]	HO ₂ · [cm ⁻³]	Nr	RO ₂ · [cm ⁻³]	HO ₂ · [cm ⁻³]	(RO _{2*(HO2)} [cm ⁻³])	(HO _{2*(HO2)} [cm ⁻³])	
J1	1.76·10 ⁰⁹	$9.15 \cdot 10^{06}$	N1	$1.42 \cdot 10^{10}$	$1.12 \cdot 10^{08}$	$7.60 \cdot 10^{09}$	$1.05 \cdot 10^{09}$	
J2	$1.58 \cdot 10^{09}$	$8.57 \cdot 10^{06}$	N2	$7.98 \cdot 10^{09}$	$3.15 \cdot 10^{08}$	$4.31 \cdot 10^{09}$	$1.62 \cdot 10^{09}$	
Ј3	$2.20 \cdot 10^{09}$	$1.60 \cdot 10^{07}$	N3	$4.33 \cdot 10^{09}$	$5.97 \cdot 10^{08}$	$3.11 \cdot 10^{09}$	$2.06 \cdot 10^{09}$	
J4	$4.33 \cdot 10^{09}$	$4.17 \cdot 10^{07}$	N5	$2.73 \cdot 10^{09}$	$7.02 \cdot 10^{08}$	$2.57 \cdot 10^{09}$	$1.93 \cdot 10^{09}$	
J5	$5.18 \cdot 10^{09}$	$5.39 \cdot 10^{07}$	N5	$1.41 \cdot 10^{09}$	$5.64 \cdot 10^{08}$	$1.76 \cdot 10^{09}$	$1.98 \cdot 10^{09}$	
J6	$5.88 \cdot 10^{09}$	$6.23 \cdot 10^{07}$	N6	$1.40 \cdot 10^{09}$	$5.61 \cdot 10^{08}$	$1.79 \cdot 10^{09}$	$2.08 \cdot 10^{09}$	
J7	$6.08 \cdot 10^{09}$	$6.81 \cdot 10^{07}$	N7	$1.08 \cdot 10^{09}$	$4.71 \cdot 10^{08}$	$1.53 \cdot 10^{09}$	$1.88 \cdot 10^{09}$	
Ј8	$6.56 \cdot 10^{09}$	$7.29 \cdot 10^{07}$	N8	$6.58 \cdot 10^{08}$	$3.05 \cdot 10^{08}$	$1.15 \cdot 10^{09}$	$1.40 \cdot 10^{09}$	
Ј9	$6.11 \cdot 10^{09}$	$7.26 \cdot 10^{07}$	N9	$4.94 \cdot 10^{08}$	$2.31 \cdot 10^{08}$	$9.25 \cdot 10^{08}$	$1.22 \cdot 10^{09}$	
J10	$6.48 \cdot 10^{09}$	$7.63 \cdot 10^{07}$	N10	$4.1 \cdot 10^{08}$	$1.9 \cdot 10^{08}$	$7.4 \cdot 10^{08}$	$9.2 \cdot 10^{08}$	
J11	$6.54 \cdot 10^{09}$	$7.93 \cdot 10^{07}$	N11	$1.78 \cdot 10^{08}$	$8.12 \cdot 10^{07}$	$2.74 \cdot 10^{08}$	$2.78 \cdot 10^{08}$	
J12	$6.60 \cdot 10^{09}$	$8.22 \cdot 10^{07}$						
C1	$1.40 \cdot 10^{09}$	$2.83 \cdot 10^{09}$						

120 S4. Additional information to the OH· reference system

Family contributions

135

140

In Figure S5 we document, as function of the turnover of α -pinene with OH·, the signal for all family members that entered the families shown in Figure 2 of the main manuscript.

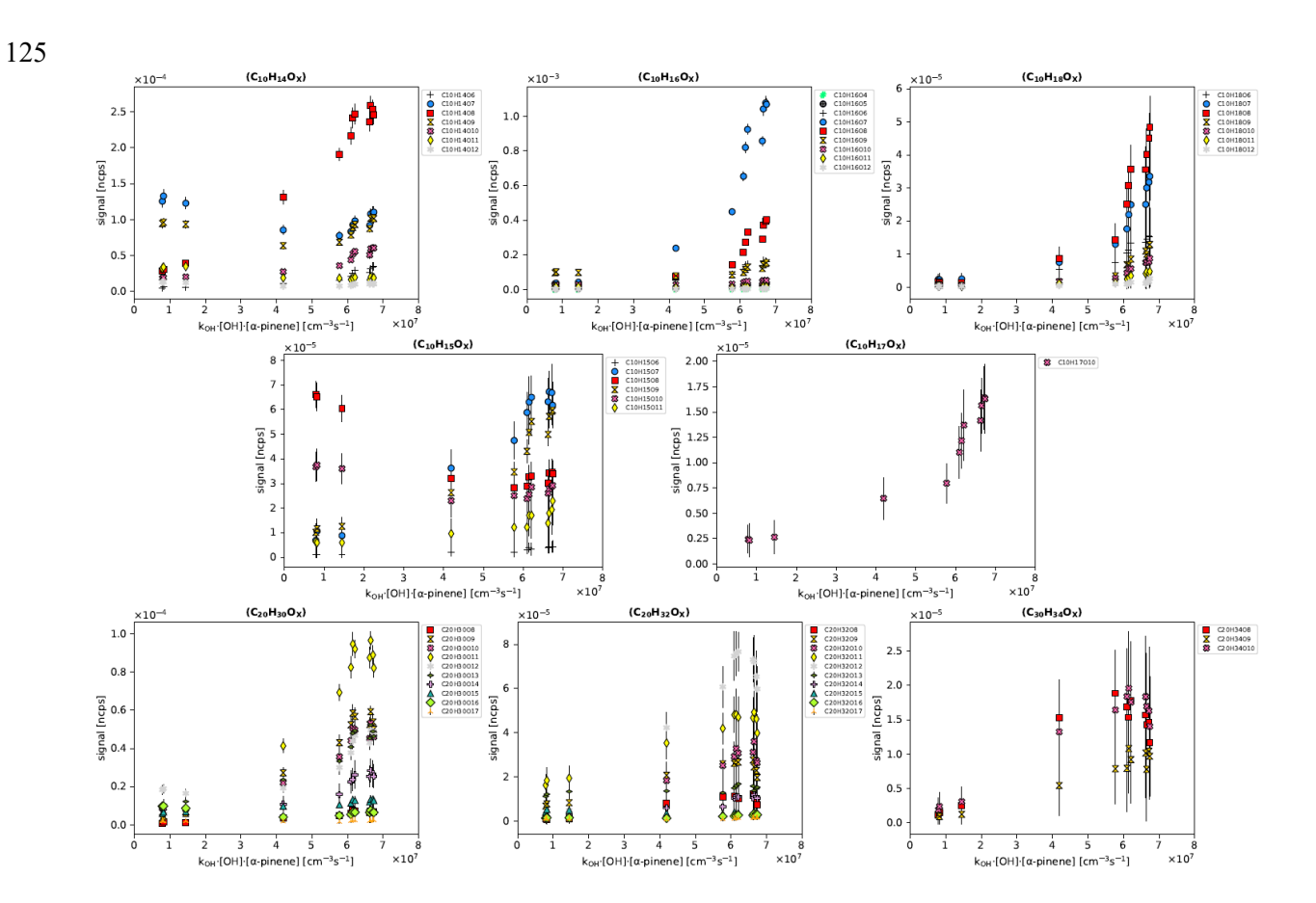


Figure S5: Signal versus turnover for monomer C₁₀ family members with closed shell compounds (top panels) and peroxy radical (middle panels) and accretion products C₂₀ family members (bottom panel). Compounds with the same number of oxygen atoms are shown with the same color and marker. The signal is normalized by the total ion count and corrected for loss to particles. Standard deviations for averaging over the steady state intervals are shown.

Rate limiting initial reactions for formation of C₁₀H₁₅O_X- and C₁₀H₁₇O_X HOM-RO₂-

The reaction with OH· is the rate limiting step in photooxidation of α -pinene by OH·. Addition of OH· to the double bond is the fastest reaction. OH· can also add to α -pinene under opening of the four-membered ring with a branching of about 10%. Both addition reactions result in $C_{10}H_{17}O_2$ radicals and according to Xu et al. (2019) the four-membered ring opening pathway leads to $C_{10}H_{17}O_X$ HOM-RO₂·. H-abstraction by OH· constitutes another pathway of α -pinene degradation also with a branching ratio of about 10% with respect to OH· addition. H abstraction leads to $C_{10}H_{15}O_2$ radicals and may be the rate limiting step to efficient HOM formation (Shen et al., 2022). $C_{10}H_{15}O_4$ radicals are formed on the vinylhydroperoxide path in α -pinene ozonolysis (Johnson and Marston, 2008). In evolved chemical systems prevailing in the daytime atmosphere and in our steady state reaction chamber $C_{10}H_{15}O_4$

radicals are also formed by H abstraction from first generation oxidation products, e.g. the major product pinal ($C_{10}H_{16}O_2$).

150

155

160

165

According to the generic HOM formation scheme in the main manuscript, autoxidation should maintain the number of carbon and hydrogen atoms of the starting peroxy radical, so we expect the $C_{10}H_{17}O_X$ and $C_{10}H_{15}O_X$ HOM-RO₂· families, which are observed. The relative importance of these reaction pathways is shown in Figure S6; the data were taken from the model calculations described in Supplement section 3.

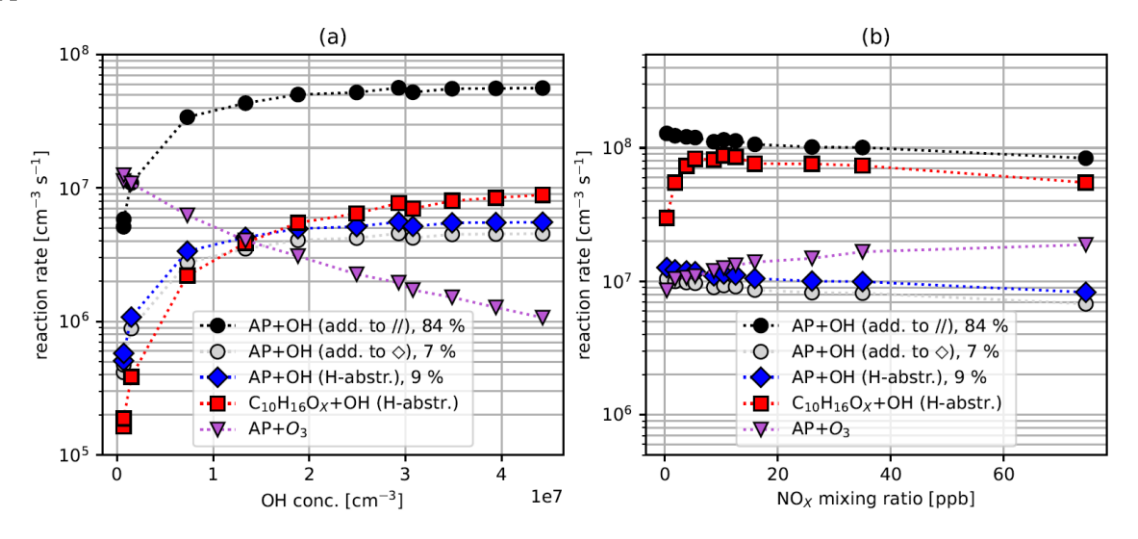


Figure S6: Importance of OH· reaction pathways for RO₂· production. Panel (a) shows the reaction rates as a function of $[OH\cdot]_{ss}$ for the reference experiments J1-J12, while panel (b) shows the results for the NO_X experiments N1-N11 as a function of NO addition. Black: OH· addition to α-pinene double bond; grey: OH· addition under breakage of the four-membered ring (menthene path); blue: H-abstraction from a-pinene; red: secondary oxidation by H-abstraction from $C_{10}H_{16}O_3$ first generation products. The reaction rate for addition of O_3 to the α-pinene double bond is given for comparison in lilac.

In the OH· reference systems (J1-J12, N1) and at low $[NO_X]_{ss}$ (N2-N4) OH· addition to the double bond (black circles) is by far the most dominant path. The OH· addition under opening of the four-membered ring (grey circles) leading to $C_{10}H_{17}O_X$ HOM-RO₂· is of similar importance as the H-abstraction from α -pinene (blue diamonds) leading to $C_{10}H_{15}O_X$ HOM-RO₂· However, the major HOM-RO₂· family found in our system is $C_{10}H_{15}O_X$.

At no- and low-NO_X, H-abstraction from α -pinene and secondary oxidation of $C_{10}H_{16}O_X$ are of about same importance, both leading to $C_{10}H_{15}O_X$ HOM-RO₂·. However, in the presence of NO_X (N5-N11), secondary oxidation becomes by far the most important $C_{10}H_{15}O_X$ source. Under conditions of efficient photooxidation (J6-J12, N1-11), ozonolysis (lilac triangles) is not a competitive source of $C_{10}H_{15}O_X$ HOM-RO₂·.

OH· generated C₁₀H₁₈O_X products

In Figure S7 we compare the signals of $C_{10}H_{17}O_{10}$ and related products $C_{10}H_{18}O_X$ as function of the turnover of α -pinene with OH·. The signal traces were normalized by the Frobenius vector norm to highlight the typical functional behavior, independent of the actual abundance. All compounds shown here can only arise from $C_{10}H_{17}O_3$, thus from addition of OH· to α -pinene. The comparison to $C_{10}H_{15}O_6$ · shows that it is not much formed in oxidation by O_3 but arises mainly also from oxidation by OH· addition.

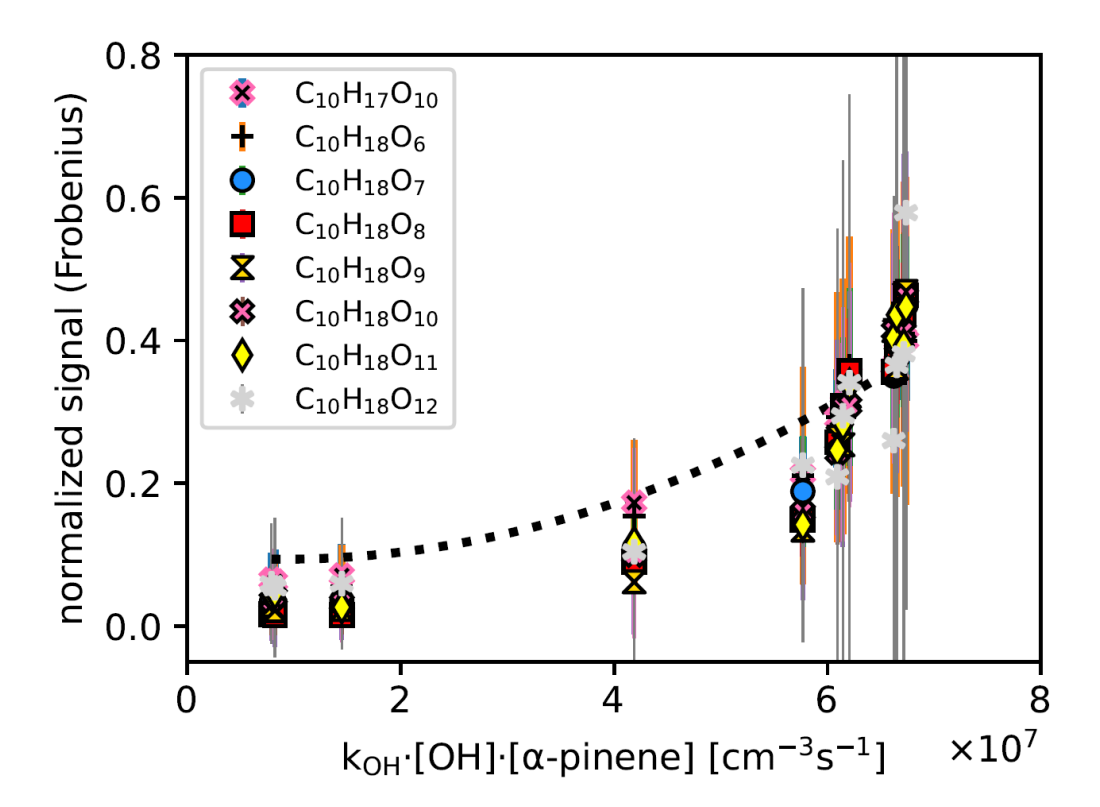


Figure S7: Signal of C₁₀H₁₇O₁₀ and C₁₀H₁₈O_X family members normalized by their vector norm as a function of the α-pinene turnover with OH·. These compounds can only originate from oxidation by OH-addition and the shape of the curves shows a monotonic increase with the turnover. The dotted line indicates the shape of the C₁₀H₁₅O_{2n+1} peroxy radical family and the C₁₀H₁₅O₆ peroxy radical as given in Figure 3 c, d. Those peroxy radicals also originate from oxidation by OH· addition. At the same time the offset at low OH· turnover indicates that the group of C₁₀H₁₅O_{2n+1} radicals must have a small ozonolysis source, too. Errors are calculated by error propagation based on the standard deviations of averaging over the steady state intervals.

S5. Fragmentation related products in the NO_X system

190

195

200

205

220

Figure S8a shows signal intensities of HOMs that underwent a fragmentation step, as function of NO_X (monomers: black circles, accretion products: blue squares). Signals of fragmented monomers (C_5 - C_9) increase with $[NO_X]_{ss}$ as expected, since fragmentation increases with alkoxy radical fromation. Fragmented accretion products decrease like C_{20} products, because dimerisation HOM-RO₂· + (HOM-)RO₂· cannot compete with HOM-RO₂· + NO. However, the fraction of the fragmented accretion products (C_{11} - C_{19}) still increases with $[NO_X]_{ss}$ (Fig S8b). Absolute increase of C_5 - C_9 HOMs and relative increase of C_{11} - C_{19} HOMs underline the importance of HOM-RO·.

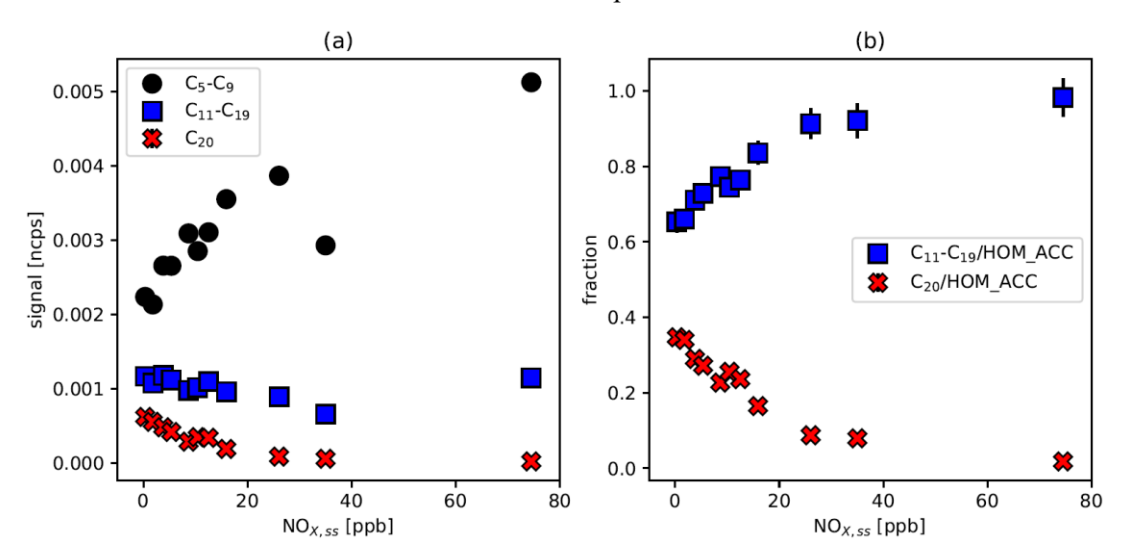


Figure S8: (a) Particle and turnover corrected signal of fragmented monomers (black circles) and fragmented accretion products (blue squares) and non-fragmented C_{20} accretion products (red crosses) as a function of $[NO_X]_{ss}$. The signal of the fragmented monomers increased with $[NO_X]_{ss}$, in accordance with increasing alkoxy radical formation. The signal of the fragmented accretion products decreased similarly to that of the non-fragmented C_{20} accretion products, however less distinct. This is caused by the increasing $[NO_X]_{ss}$ suppressing overall the accretion product formation due to the fast reaction of HOM- RO_2 with NO. (b) The fraction of fragmented accretion products (normalized to the total signal of all HOM-ACC) increased with NO_X , indicating that the fragmented accretion products also reflected an increase of alkoxy radical formation. Errors are calculated by error propagation based on the standard deviations of averaging over the steady state intervals.

S6. Kinetic considerations

Estimation of the branching ratio for isomerization of HOM-RO·

Figure 3b of the main manuscript shows the fraction of the C₁₀H₁₅O_X· with odd oxygen numbers that have undergone an alkoxy-step with subsequent isomerization by H-shift under retaining the C₁₀-backbone. As a consequence, the same fraction of their termination products, non-fragmented HOM monomers, C₁₀H₁₄O_X and C₁₀H₁₆O_X (Fig. 2b), as well as HOM-ACC, C₂₀H₃₀O_X and C₂₀H₃₂O_X (Fig. 2c), must have also undergone an alkoxy step followed by isomerization. On the other hand, the fragmented monomers and fragmented accretion products shown in Figure 2d have undergone alkoxy steps with subsequent fragmentation. Note, both C₁₀H₁₅O_X peroxy radicals and fragmented HOM-RO₂·, with C₅-C₉, can be trapped in fragmented HOM-ACC.

By rationing the signals of non-fragmented HOM and fragmented HOM in a suited way we can roughly estimate the branching ratio into isomerization (f_{iso}) and fragmentation for HOM-RO· ($C_{10}H_{15}O_{X-1}$ ·) by (S5):

$$f_{iso} = \frac{f_{alk} \cdot \sum_{i} [non-fragmented\ product]_{ss,i}}{f_{alk} \cdot \sum_{i} [non-fragmented\ product]_{ss,i} + f_{alk} \cdot \sum_{j} [fragmented\ product]_{ss,j}} \ \ (S5)$$

with the fraction of HOM that were formed involving an alkoxy-peroxy step (falk) given by (S6)

225
$$f_{alk} = \frac{[C_{10}H_{15}O_{2n+1}]_{ss}}{[C_{10}H_{15}O_X]_{ss}}$$
 (S6)

Herein, we used normalized signals as a measure for concentrations, assuming similar sensitivities.

Note, an inherent uncertainty will persist in f_{iso} , because $C_{10}H_{15}O_{X'}$ as well as fragmented HOM-RO₂· are trapped in HOM-ACC in various combinations. Moreover, conventional C_{10} -RO₂· (here, mainly $C_{10}H_{17}O_{3}$ ·, and $C_{10}H_{15}O_{4}$ ·) can be also trapped in C_{20} -HOM-ACC if their concentration is sufficiently large (Berndt et al., 2018b, McFiggans et al., 2019, Pullinen et al., 2020). The abundance of a specific HOM-ACC is of course not only dependent on the concentration of both peroxy radicals involved in the accretion reaction, but also on the rate coefficient for the specific accretion reaction, which we cannot assess yet. Therefore, treatment of the HOM-ACC beyond simple permutation remains a challenge which we cannot resolve unambiguously at the moment. Instead, we construct minimum and maximum estimates for f_{iso} by making plausible guesses for minimum and maximum number of $C_{10}H_{15}O_{X'}$ or fragmented HOM-RO₂· entities that could have been trapped in specific HOM-ACC families (Table S4). The number of entities multiplied by the signal of the family was then considered in the according sums in (S5).

Table S4: Entities of C₁₀H₁₅O_X and C₅-C₉-RO₂ in HOM monomers and HOM-ACC

Non-f	ragmented entit	ies	Fra	gmented entiti	es
HOM group	max	min	HOM group	max	min
$C_{10}H_{14}O_{X}$	1	1	C ₅ -C ₆ HOM	1	1
$C_{10}H_{16}O_{X}^{a)}$	1	1			
$C_{20}H_{30}O_{2n+1}{}^{b)}\\$	1	1			
$C_{20}H_{30}O_{2n}^{\ c)}$	2	1			
$C_{20}H_{32}OX^{d)}\\$	1	1 ^{f)}			
$C_{19}H_YO_X{^e)}$	2	1	$C_{19}H_YO_X$	1 ^{f)}	$0^{e)}$
$C_{18}H_YO_X{^e)}$	2	0	$C_{18}H_YO_X{}^{g)}\\$	2	0
$C_{17}H_YO_X^{e)}$	2	0	$C_{17}H_YO_X{}^{g)}$	2	0
C_{11} - $C_{16}^{f)}$	1	0	C_{11} - C_{16}	2 ^{g)}	1 ^{f)}

240

245

230

235

The rationale for the selection of minimum and maximum numbers is listed in the following with the small letters referring to Table S4:

- a) $C_{10}H_{16}O_{X-1}$ can also arise from $C_{10}H_{17}O_X$ by R3a, however we showed that such a contribution is small in our study.
- b) Recombination reaction R6 requires that one of the two RO₂· involved in the formation must have an even number of O atoms

- c) $C_{20}H_{30}O_X$ can be formed by recombination of two HOM- $C_{10}H_{15}O_X$ but can also contain a conventional RO_2 entity.
- d) a $C_{10}H_{17}O_X$ radical must be involved either HOM-RO₂ or conventional RO₂.

255

265

270

- e) Peräkyla et al. (2023) showed that such fragmented HOM-ACC can result in decay of intermediate tetroxides, which could have been formed by two C₁₀H₁₅O_X· entities. In any case one C₁₀H₁₅O_X·entity must be involved, since [C₁₀H₁₇O_X·]_{ss} is negligible under our conditions.
- f) Besides case e) fragmented C₁₇-C₁₉ HOM-ACC can be formed be recombination of one C₁₀H₁₅O_X·entity and one respective fragmented C₅-C₉ HOM-RO₂·. The latter is also valid for C₁₁-C₁₆ HOM-ACC.
- g) With the exception of C₁₉-HOM-ACC, fragmented C₁₁-C₁₈-HOM-ACC can be formed by recombination of two fragmented HOM-RO₂·.

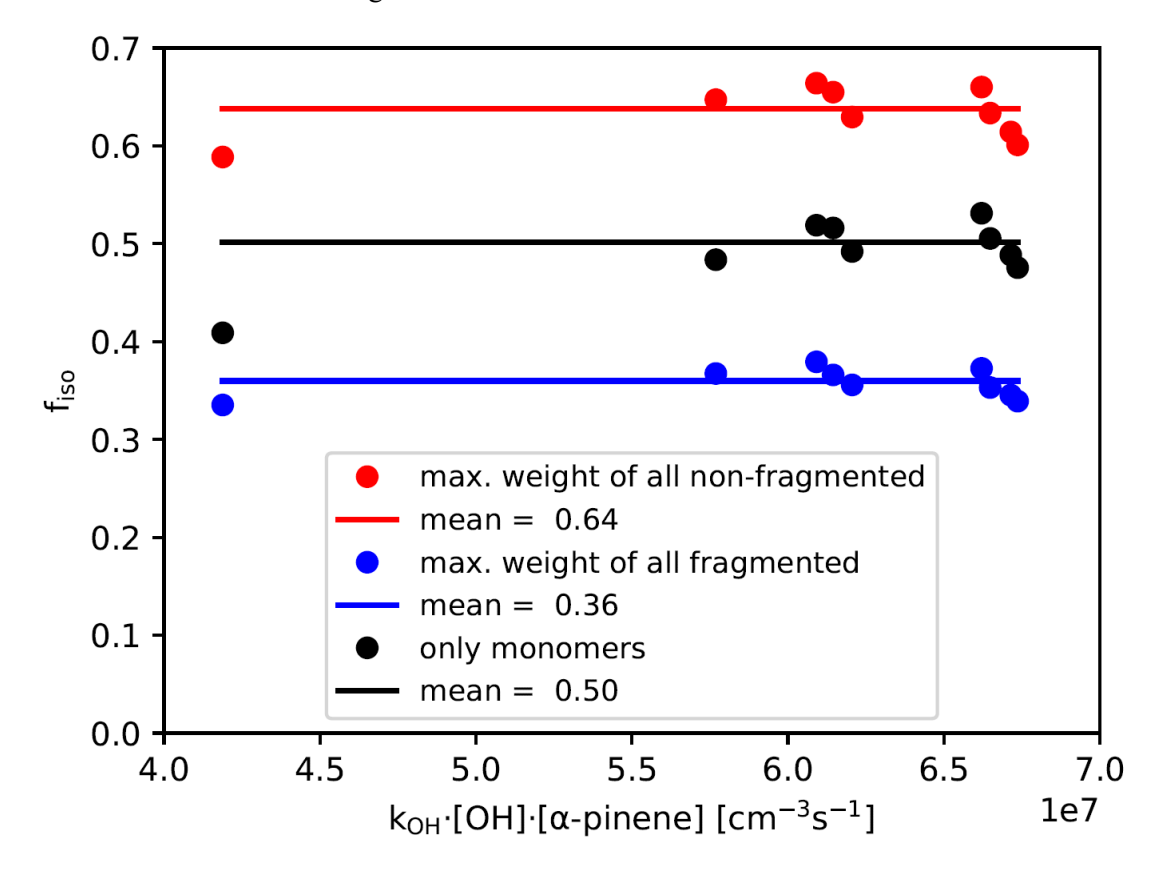


Figure S9: Branching ratio into isomerization for HOM-RO· (f_{iso}) as a function of the α-pinene turnover with OH· with more than 90% of the α-pinene oxidized by OH·. Combinations maximum fragmented/minimum non-fragmented entities in HOM-ACC (blue) and minimum fragmented/maximum non-fragmented entities in HOM-ACC (red) and their means were calculated by (S5) with inputs from Table S4.

Figure S9 shows average f_{iso} as a function of the α -pinene turnover by OH·, where more than 90% of the a-pinene is converted by reaction with OH·, calculated for each steady state, as well as the average for steady states (lines in Fig. S9). The extreme cases for f_{iso} shown in Figure S9 span some range, but f_{iso} is in each case not dependent on the turnover, as it should be.

We also show in Figure S9 f_{iso} calculated only considering the monomer HOMs and neglecting the (more uncertain) contribution of HOM-ACC to the budgets. The non-fragmented monomers make up a fraction of about 80% of the non-fragmented HOM under regard. For the case of fragmented HOM, fragmented C_5 - C_9 monomers constitute about 55% on average. So, substantial parts of information needed to calculate f_{iso} are already provided by the monomers alone. The f_{iso} = 0.5 determined from the monomers is the same as the average of maximum and minimum f_{iso} . As expected from Table S4 the

uncertainty about trapping non-fragmented and fragmented HOM-RO₂·in HOM-ACC is causing the largest uncertainty in f_{iso}.

From our analysis, we conclude that the branching into isomerization for HOM-RO \cdot which retains the C₁₀ backbone is roughly in a range between 36% and 64% with a good likelihood being close to 50%. In other words, about half of the HOM-RO \cdot isomerize by H-shift while the other half undergoes fragmentation. This is in the range of results from theoretical kinetics (Vereecken et al. 2009; Vereecken et al. 2010). In the calculations in the main manuscript we will assume for simplicity 0.5 for the branching into isomerization and fragmentation.

Rate coefficient for the formation of HOM-NO₃

280

285

300

305

310

All observations indicate that HOM-RO₂· behave kinetically similar to conventional, small RO₂· (reviewed in Bianchi et al. 2019). That is why concepts of conventional atmospheric, organic chemistry, e.g. applied in MCMv3.1.1, can be transferred to HOMs. In the NO_X system studied here we were able to observe seven couples of HOM-RO₂· and HOM-NO₃ that are chemically related by NO addition. For steady state conditions we can calculate with some assumptions the rate coefficient for the family of reactions

$$C_{10}H_{15}O_X + NO = C_{10}H_{15}NO_{X+1}$$

In steady state, the concentration $[C_{10}H_{15}NO_{X+1}]_{ss}$ is given by equation (S7)

$$[C_{10}H_{15}NO_{X+1}]_{ss} = \frac{P}{c_{loss}}$$
 (S7)

wherein the overall production of C₁₀H₁₅NO_{X+1} (P) is given by (S8)

$$P = f_{orgNO3} \cdot k_{RO2+NO} \cdot [C_{10}H_{15}O_X]_{ss} \cdot [NO]_{ss} + P^{other}$$
 (S8)

and c_{loss} is the sum of the (pseudo-) first order loss *coefficients* of C₁₀H₁₅NO_{X+1} as given by (S9).

295
$$c_{loss} = k_{wall} + k_{OH} \cdot [OH \cdot]_{ss} + j_{UV} + k_{dil}$$
 (S9)

In (S8) k_{RO2+NO} is the overall rate coefficient for the reaction of HOM-RO₂· with NO and f_{orgNO3} the branching ratio into HOM-NO₃. (The branching into HOM-RO· is then given by 1- f_{orgNO3} .). In principle we must allow for other formation processes P^{other} leading to $C_{10}H_{15}NO_{X+1}$. Since we are using HR-MS for detection without speciation, this also includes production processes leading to structure isomers with the same formula. (In our system candidates would be PAN-like HOM peroxyacyl nitrates which could be formed by $C_{10}H_{15}O_{X-1} + NO_2$ but are likely thermally not very stable.)

In (S9) k_{wall} is the wall loss rate coefficient for HOMs, which was measured and where the minimum lifetime due to wall loss amounts to 120 s. Wall losses of the HOMs are faster by about a factor of 20 than the losses caused by the flow out of the chamber ($k_{dil} \approx 0.0004 \text{ s}^{-1}$, $\tau_{dil} \approx 2500 \text{ s}$).

In principle we should allow for photolysis of $C_{10}H_{15}NO_{X^{+1}}$ with photolysis frequency j_{UV} and for reaction with OH^{\cdot} with a rate coefficient k_{OH} . However, the fastest photolysis frequencies in our system (J_{NO2} and J_{10D}) are about $1.3\cdot10^{-3}$ s⁻¹ and $2.5\cdot10^{-3}$ s⁻¹, respectively. Photolysis frequencies for organic compounds are at least one order of magnitude smaller, for example, photolysis frequencies of organic nitrates, J_{51} - J_{56} , in MCMv3.3.1 are in a range of about $3\cdot10^{-8}$ - $3\cdot10^{-5}$ s⁻¹ for the light conditions in our chamber. So, the lifetime of HOM-NO₃ with respect to photolysis is likely much longer than 4000 s, rendering it ineffective. In contrast, reaction of $C_{10}H_{15}NO_{X^{+1}}$ with OH^{\cdot} at the collision limit $k_{OH} \approx 1\cdot10^{-10}$ cm³ s⁻¹ would yield lifetimes in a range of 150-250 s.

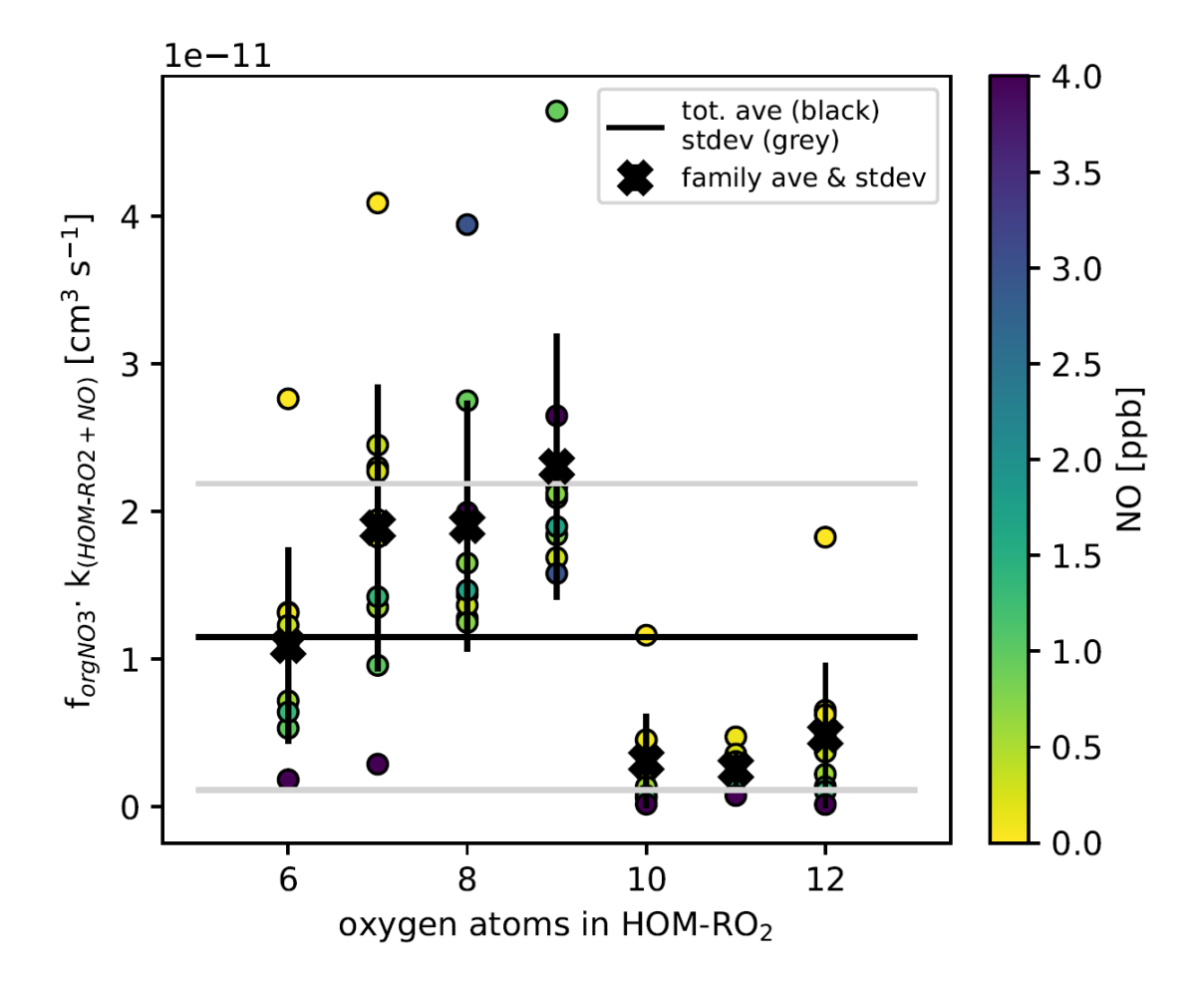


Figure S10: Rate coefficients calculated for reactions $C_{10}H_{15}O_{X^-} + NO \rightarrow C_{10}H_{15}O_{X^-2}$ -ONO₂ as a function of the number of oxygen atoms in $C_{10}H_{15}O_{X^-}$. The rate coefficients were calculated directly from the observations. The rate coefficients are the product of the overall rate coefficients for $C_{10}H_{15}O_X + NO$ and the branching ratio into organic nitrates HOM-NO₃ f_{orgNO3} . The approach comprises an unknown degree of lumping since a specific $C_{10}H_{15}O_Z$ signal can cover more than one structure isomer. The actual steady state NO is indicated by the color code. Black crosses show the family average and black bars its standard deviation. The black line is the average over all families with the grey lines indicating the standard deviation.

Wall loss ($\tau_{wall} = 120$ s) is thus the dominant loss path of HOMs in the chamber and we can neglect other loss terms but the loss by OH reactions in (S9). If we also neglect "other" production pathways the balance equation for $C_{10}H_{15}NO_{X+1}$ simplifies to (S10)

$$[C_{10}H_{15}NO_{X+1}]_{ss} = \frac{f_{orgNO3} \cdot k_{RO2+NO} \cdot [C_{10}H_{15}O_X]_{ss} \cdot [NO]_{ss}}{k_{wall} + k_{OH} \cdot [OH \cdot]_{ss}}$$
(S10)

and we can isolate $f_{orgNO3} \cdot k_{RO2+NO}$ as given by (S11):

315

320

335

330
$$f_{orgNO3} \cdot k_{RO2+NO} = \frac{k_{wall} + k_{OH} \cdot [OH \cdot]}{[NO]_{ss}} \cdot \frac{[C_{10}H_{15}NO_{X+1}]_{ss}}{[C_{10}H_{15}O_{X+1}]_{ss}}$$
(S11)

We assumed reaction with OH· at the collision limit and set $k_{OH} = 10^{-10}$ cm³ s⁻¹. All other terms at the right side were determined experimentally.

Figure S10 shows the rate coefficients for the formation of HOM-NO₃ for all observed peroxy/nitrate couples at each $[NO_X]_{ss}$ condition (indicated by the color code) as a function of the oxidation degree of the HOM-RO₂. Also shown are the average rate coefficient for each couple over all $[NO_X]_{ss}$ conditions (black crosses) with 1σ error bars as well as the overall average (black line) with 1σ error

bounds (grey lines). There is a tendency to higher $f_{orgNO3} \cdot k_{RO2+NO}$ at lower $[NO_X]_{ss}$ conditions. This could have two reasons, i) the isomeric composition changes substantially with $[NO_X]_{ss}$, ii) a neglected production term, e.g. with NO_2 , contributes relatively more to the formation of $C_{10}H_{15}NO_{X+1}$ at lower $[NO_X]_{ss}$.

The overall rate coefficient $f_{orgNO3} \cdot k_{RO2+NO}$ amounts to $1.15(\pm 1.0) \cdot 10^{-11}$ cm³ s⁻¹. If one neglects the loss by OH· reactions, $f_{orgNO3} \cdot k_{RO2+NO}$ would become $7(\pm 6) \cdot 10^{-12}$ cm³ s⁻¹. Note, the large uncertainty is mainly due to lumping. Even at a given number of oxygen atoms the structure isomer mix for the same formula can vary with $[NO_X]_{ss}$. Furthermore, compounds with different numbers of oxygen atoms do not necessarily have the same rate coefficients. Figure S10 indicates thus more the span of possible rate coefficients.

Our average rate coefficient $f_{orgNO3}\cdot k_{RO2+NO}$ can be compared against the k_{RO2NO} applied for the overall reaction $RO_2\cdot +NO$ (R4 and R8) in model calculations by MCMv3.3.1. Therein $\approx 9.5\cdot 10^{-12}$ cm³ s⁻¹ is used which multiplied by the average branching ratio of 0.14 into organic nitrates (R4) results in $1.3\cdot 10^{-12}$ cm³ s⁻¹. The MCMv3.1.1 tends to underestimate the organic nitrate formation and we have shown for β -pinene an average branching ratio of 0.36 compared to 0.14 in MCMv3.1.1 (Pullinen et al. 2020). Applying 0.36 for the branching ratio into organic nitrates, the rate coefficient in MCM would become $3.5\cdot 10^{-12}$ cm³ s⁻¹, which is within a factor of ~ 3 of our estimate, well within our error margins.

Competition of a two step alkoxy-peroxy path and autoxidation

- We show in the main manuscript that the alkoxy-peroxy path is able to compete with autoxidation whenever the isomerization rate of a specific HOM-RO₂· is slower than its bimolecular reaction rate with NO or other RO₂· (Fig. 9). The alkoxy-peroxy path allows for continuation of the radical chain under keeping the carbon backbone by alkoxy isomerization, thus enabling continuation of autoxidation via the resulting new HOM-RO₂.
- We can construct a case wherein we can directly investigate the competition of two alkoxy-peroxy steps with a single autoxidation step leading to the same formula compound. Starting from a specific HOM-RO₂·, two alkoxy-peroxy steps can lead to a higher oxidized HOM-RO₂· with the same formula as one step of autoxidation (shown in main manuscript, Fig. 8). For two alkoxy-peroxy steps to be competitive with direct autoxidation we assume a negligible autoxidation rate for the intermediate HOM-RO₂·, otherwise it would continue the autoxidation chain as sketched above.

To compare directly the competitiveness of two alkoxy-peroxy steps and autoxidation, we apply the following reaction equations using the same labeling as in Fig. 8 of the main manuscript.

Autoxidation:

340

345

350

380

$$HOM-RO_2$$
 · A H -shift $+O_2 \rightarrow HOM-RO_2$ · B (route 1)

Formation of peroxy radical (HOM-RO₂·^B) from precursor peroxy radical (HOM-RO₂·^A) after two alkoxy-peroxy steps:

 HOM-RO_2 . A reaction with NO, RO_2 . \rightarrow HOM-RO. (route 2)

 $HOM-RO^{\cdot C} H-shift + O_2 \rightarrow HOM-RO_2^{\cdot D}$ (route 3)

HOM-RO^{⋅C} fragmentation →loss (not shown in Fig. 8)

375 HOM-RO₂·D reaction with NO, RO₂· \rightarrow HOM-RO·E (route 4)

 $HOM-RO^{\cdot E} H-shift + O_2 \rightarrow HOM-RO_2^{\cdot B}$ (route 5)

 $HOM-RO^{B}$ fragmentation $\rightarrow loss$ (not shown in Fig. 8)

Based on these reaction equations we derive the following equations for steady state conditions.

The steady state concentration of the first alkoxy radical HOM-RO^{.C} can be expressed by the ratio of its production rate and its loss coefficients for isomerization and fragmentation

$$[HOM-RO^{\cdot C}]_{SS} = \frac{(0.6 \cdot k_{RO2+RO2} \cdot [RO_2^{\cdot T}]_{SS} + 0.64 \cdot k_{RO2+NO} \cdot [NO]_{SS}) \cdot [HOM-RO_2^{\cdot A}]_{SS}}{k_{iso} + k_{frag}}$$
(S12)

wherein $k_{RO2+RO2}$ and k_{RO2+NO} are the rate coefficients for reaction of RO_2 with RO_2 and RO_2 and RO_2 are the rate coefficients for alkoxy isomerization and fragmentation. The branching into alkoxy radicals of 0.6 and 0.64 were derived from Jenkin et al. (2019) and taken from Pullinen et al. (2020), respectively.

The steady state concentration of the second peroxy radical (HOM-RO₂·^D) formed from the alkoxy radical HOM-RO·^C is given in the same sense by

$$[HOM - RO_2^{D}]_{SS} = \frac{k_{iso} \cdot [HOM - RO^{C}]_{SS}}{k_{RO2 + RO2} \cdot [RO_2^{T}]_{SS} + k_{RO2 + NO} \cdot [NO]_{SS}}$$
(S13)

Remember, we set the autoxidation of HOM-RO₂. D to be negligible.

Replacing [HOM-RO·^C]_{ss} in (S13) by (S12):

385

$$[\text{HOM-RO}_{2}^{D}]_{SS} = \frac{k_{iso}}{k_{iso} + k_{frag}} \cdot \frac{(0.6 \cdot k_{RO2 + RO2} \cdot [RO_{2}^{\cdot T}]_{SS} + 0.64 \cdot k_{RO2 + NO} \cdot [NO]_{SS}) \cdot [HOM \cdot RO_{2}^{\cdot A}]_{SS}}{k_{RO2 + RO2} \cdot [RO_{2}^{\cdot T}]_{SS} + k_{RO2 + NO} \cdot [NO]_{SS}}$$
(S14)

In analogy, the steady state concentration of the second alkoxy radical HOM-RO.^E is given by:

$$[HOM-RO^{\cdot E}]_{SS} = \frac{(0.6 \cdot k_{RO2+RO2} \cdot [RO_2^{\cdot T}]_{SS} + 0.64 \cdot k_{RO2+NO} \cdot [NO]_{SS}) \cdot [HOM-RO_2^{D \cdot}]_{SS}}{k_{ISO} + k_{frag}}$$
(S15)

By replacing [HOM-RO₂·D]_{ss} in (S15) by (S14) follows:

$$[HOM-RO^{\cdot E}]_{SS} = \frac{k_{iso}}{(k_{iso} + k_{frag})^2} \cdot \frac{(0.6 \cdot k_{RO2+RO2} \cdot [RO_2^{\cdot T}]_{ss} + 0.64 \cdot k_{NO} \cdot [NO]_{ss})^2 \cdot [HOM-RO_2^{\cdot A}]_{ss}}{k_{RO2+RO2} \cdot [RO_2^{\cdot T}]_{ss} + k_{RO2+NO} \cdot [NO]_{ss}}$$
(S16)

Finally, the steady state concentration of the target peroxy radical HOM-RO₂.^B formed via alkoxy-peroxy path is given by:

$$[HOM - RO_2^{\cdot B}]_{SS} = \frac{k_{iso} \cdot [HOM - RO^{\cdot E}]_{SS}}{k_{RO2 + RO2} \cdot [RO_2^{\cdot T}]_{SS} + k_{RO2 + NO} \cdot [NO]_{SS}}$$
(S17)

Replacing [HOM-RO·E]_{ss} in (S17) by (S16):

$$[HOM-RO_2^{\cdot B}]_{SS} = \frac{k_{iso}^2}{(k_{iso} + k_{frag})^2} \cdot \frac{(0.6 \cdot k_{RO2+RO2} \cdot [RO_2^{\cdot T}]_{SS} + 0.64 \cdot k_{RO2+NO} \cdot [NO]_{SS})^2 \cdot [HOM-RO_2^{\cdot A}]_{SS}}{(k_{RO2+RO2} \cdot [RO_2^{\cdot T}]_{SS} + k_{RO2+NO} \cdot [NO]_{SS})^2}$$
(S18)

In order to compare production via two alkoxy-peroxy steps with production by autoxidation, we need to derive the production P(HOM-RO₂·B) from (S18). The production rate is given by the steady state concentration multiplied by the sum of the loss coefficients (S19)

$$loss = k_{RO2+RO2} \cdot \left[RO_2^{\cdot T} \right]_{ss} + k_{RO2+NO} \cdot [NO]_{ss}$$
 (S19)

and amounts to

$$P(HOM-RO_{2}^{\cdot B}) = \left(\frac{k_{iso}}{k_{iso} + k_{frag}}\right)^{2} \cdot \frac{(0.6 \cdot k_{RO2+RO2} \cdot [RO_{2}^{\cdot T}]_{ss} + 0.64 \cdot k_{RO2+NO} \cdot [NO]_{ss})^{2}}{k_{RO2+RO2} \cdot [RO_{2}^{\cdot T}]_{ss} + k_{RO2+NO} \cdot [NO]_{ss}} \cdot \left[HOM-RO_{2}^{\cdot A}\right]_{ss}$$
(S20)

By comparison of the rate coefficients in (S20), the effective pseudo first order rate coefficient k_{eff} for the production of HOM-RO₂.^B from HOM-RO₂.^A by a two consecutive alkoxy-peroxy steps is given by (S21).

$$k_{eff} = f_{iso}^{2} \cdot \frac{(0.6 \cdot k_{RO2 + RO2} \cdot [RO_{2}^{T}]_{ss} + 0.64 \cdot k_{NO}[NO]_{ss})^{2}}{k_{RO2 + RO2} \cdot [RO_{2}^{T}]_{ss} + k_{RO2 + NO} \cdot [NO]_{ss}}$$
(S21)

Herein the first factor simplifies because it is solely determined by the branching ratio for isomerization f_{iso} and fragmentation f_{frag} , and by definition $f_{frag} = 1 - f_{iso}$.

The k_{eff} derived in (S21) is a function of [NO]_{ss} and [RO₂·^T]_{ss}. It is used in section 3.4 in the main manuscript, where we compare the importance of alkoxy-peroxy pathways and autoxidation.

References

- Berndt, T., Richters, S., Kaethner, R., Voigtlaender, J., Stratmann, F., Sipilae, M., Kulmala, M., and Herrmann, H.: Gas-Phase Ozonolysis of Cycloalkenes: Formation of Highly Oxidized RO₂ Radicals and Their Reactions with NO, NO₂, SO₂, and Other RO₂ Radicals, Journal of Physical Chemistry A, 119, 10336-10348, 10.1021/acs.jpca.5b07295, 2015.
- Ehhalt, D.H.: Chemical reactions in the troposphere, in: Global Aspects of Atmospheric Chemistry, edited by: Zellner, R. G. E., Topics in Physical Chemistry, Steinkopff, Darmstadt, 60-94, 1999.
 - Fuchs, H., Tan, Z., Lu, K., Bohn, B., Broch, S., Brown, S. S., Dong, H., Gomm, S., Häseler, R., He, L., Hofzumahaus, A., Holland, F., Li, X., Liu, Y., Lu, S., Min, K. E., Rohrer, F., Shao, M., Wang, B., Wang, M., Wu, Y., Zeng, L., Zhang, Y., Wahner, A., and Zhang, Y.: OH reactivity at a rural site (Wangdu) in the North China Plain: contributions from OH reactants and experimental OH budget, Atmos. Chem. Phys., 17, 645-661, 10.5194/acp-17-645-2017, 2017.
 - Jenkin, M. E., Valorso, R., Aumont, B., and Rickard, A. R.: Estimation of rate coefficients and branching ratios for reactions of organic peroxy radicals for use in automated mechanism construction, Atmos. Chem. Phys., 19, 7691-7717, 10.5194/acp-19-7691-2019, 2019.
- Pullinen, I., Schmitt, S., Kang, S., Sarrafzadeh, M., Schlag, P., Andres, S., Kleist, E., Mentel, T. F.,
 Rohrer, F., Springer, M., Tillmann, R., Wildt, J., Wu, C., Zhao, D., Wahner, A., and Kiendler-Scharr,
 A.: Impact of NO_X on secondary organic aerosol (SOA) formation from α-pinene and β-pinene photooxidation: the role of highly oxygenated organic nitrates, Atmos. Chem. Phys., 20, 10125-10147, 10.5194/acp-20-10125-2020, 2020.
- Shen, H., Vereecken, L., Kang, S., Pullinen, I., Fuchs, H., Zhao, D., and Mentel, T. F.: Unexpected significance of a minor reaction pathway in daytime formation of biogenic highly oxygenated organic compounds, Science Advances, 8, eabp8702, doi:10.1126/sciadv.abp8702, 2022.
 - Slater, E. J., Whalley, L. K., Woodward-Massey, R., Ye, C., Lee, J. D., Squires, F., Hopkins, J. R., Dunmore, R. E., Shaw, M., Hamilton, J. F., Lewis, A. C., Crilley, L. R., Kramer, L., Bloss, W., Vu, T., Sun, Y., Xu, W., Yue, S., Ren, L., Acton, W. J. F., Hewitt, C. N., Wang, X., Fu, P., and Heard, D. E.:
- Elevated levels of OH observed in haze events during wintertime in central Beijing, Atmos. Chem. Phys., 20, 14847-14871, 10.5194/acp-20-14847-2020, 2020.
 - Tan, Z. F., Fuchs, H., Lu, K. D., Hofzumahaus, A., Bohn, B., Broch, S., Dong, H. B., Gomm, S., Häseler, R., He, L. Y., Holland, F., Li, X., Liu, Y., Lu, S. H., Rohrer, F., Shao, M., Wang, B. L., Wang, M., Wu, Y. S., Zeng, L. M., Zhang, Y. S., Wahner, A., and Zhang, Y. H.: Radical chemistry at a rural
- site (Wangdu) in the North China Plain: observation and model calculations of OH, HO₂ and RO₂ radicals, Atmospheric Chemistry and Physics, 17, 663-690, 10.5194/acp-17-663-2017, 2017.
- Tan, Z., Rohrer, F., Lu, K., Ma, X., Bohn, B., Broch, S., Dong, H., Fuchs, H., Gkatzelis, G. I., Hofzumahaus, A., Holland, F., Li, X., Liu, Y., Liu, Y., Novelli, A., Shao, M., Wang, H., Wu, Y., Zeng, L., Hu, M., Kiendler-Scharr, A., Wahner, A., and Zhang, Y.: Wintertime photochemistry in Beijing: observations of RO_X radical concentrations in the North China Plain during the BEST-ONE campaign, Atmos. Chem. Phys., 18, 12391-12411, 10.5194/acp-18-12391-2018, 2018.

Vereecken, L. and Peeters, J.: Decomposition of substituted alkoxy radicals—part I: a generalized structure—activity relationship for reaction barrier heights, Phys. Chem. Chem. Phys., 11, 9062–9074, https://doi.org/10.1039/b909712k, 2009.

- Vereecken, L. and Peeters, J.: A structure–activity relationship for the rate coefficient of H-migration in substituted alkoxy radicals, Phys. Chem. Chem. Phys., 12, 12608–12620, https://doi.org/10.1039/c0cp00387e, 2010.
- Whalley, L. K., Slater, E. J., Woodward-Massey, R., Ye, C., Lee, J. D., Squires, F., Hopkins, J. R.,
 Dunmore, R. E., Shaw, M., Hamilton, J. F., Lewis, A. C., Mehra, A., Worrall, S. D., Bacak, A.,
 Bannan, T. J., Coe, H., Percival, C. J., Ouyang, B., Jones, R. L., Crilley, L. R., Kramer, L. J., Bloss, W. J., Vu, T., Kotthaus, S., Grimmond, S., Sun, Y., Xu, W., Yue, S., Ren, L., Acton, W. J. F., Hewitt, C. N., Wang, X., Fu, P., and Heard, D. E.: Evaluating the sensitivity of radical chemistry and ozone formation to ambient VOCs and NO_X in Beijing, Atmos. Chem. Phys., 21, 2125-2147, 10.5194/acp-21-2125-2021, 2021.